

Summary of the Advanced Supersonic Parachute Inflation Research Experiment (ASPIRE) Sounding Rocket Tests with a Disk-Gap-Band Parachute

Bryan S. Sonneveldt*, Ian G. Clark[†], and Clara O'Farrell[‡]

Jet Propulsion Laboratory, California Institute of Technology, Pasadena, CA, 91106, USA

The Advanced Supersonic Parachute Inflation Research Experiments (ASPIRE) project was tasked with developing and utilizing a capability for testing full scale supersonic parachutes in Mars-relevant conditions. The initial focus was to act as a risk reduction activity for the Mars 2020 mission by testing two candidate Disk-Gap-Band (DGB) parachutes. A Terrier-Black Brant IX sounding rocket launched out of Wallops Flight Facility (WFF) in Virginia was used to deliver the two candidate parachutes to deployment and inflation conditions relevant to the Mars 2020 mission. The two candidate parachutes were a Build-to-Print version of the 21.5 meter diameter DGB parachute used for the Mars Science Laboratory (MSL) mission and a strengthened DGB parachute of the same geometry but with different materials and construction methods. Three tests took place between October 2017 to September 2018. The first flight (SR01) tested the MSL Build-to-Print DGB parachute while the second and third (SR02 and SR03) flights tested the Strengthened DGB parachute. These tests targeted a specific dynamic pressure at parachute deploy in order to reach a desired load on the parachute at full inflation. The parachutes were mortar-fire deployed at dynamic pressures ranging from 452 to 932 Pascals and Mach numbers between 1.77 and 1.97. The parachutes experienced a peak force of 32, 56, and 67 klb for SR01, SR02, and SR03 respectively. All three flights reached their desired test conditions and all parachutes survived the stresses of their supersonic deployment and inflation while showing no significant damage. All data necessary to reconstruct the performance of parachute tests, including high speed footage of inflation, was successfully obtained. This paper will present an overview of all three ASPIRE flights. This includes an explanation of the test architecture, a summary of mission operations, high level results along with brief analysis, and the conclusions from these tests. This paper also references the various technical papers that present more details about individual test results and analysis.

I. Nomenclature

C_D	=	Coefficient of Drag
C_{tot}	=	Total Force Coefficient
D_0	=	Nominal Diameter
F_{chute}	=	Force on the Parachute
F_D	=	Drag Force
M	=	Mach number
q_∞	=	Dynamic Pressure
S_0	=	Parachute Reference Area

*Systems Engineer, Entry Descent and Landing Systems & Advanced Technologies, bryan.s.sonneveldt@jpl.nasa.gov

[†]Systems Engineer, Entry Descent and Landing Systems & Advanced Technologies

[‡]Guidance and Control Engineer, Entry Descent and Landing Guidance and Control Systems

II. Introduction

A. ASPIRE Background

Each U.S. robotic mission to the Martian surface to date has used a supersonic Disk-Gap-Band (DGB) parachute to decelerate the spacecraft from supersonic to subsonic speeds as part of the descent and landing sequence. The DGB parachute design used for these missions was developed back in the 1960's and 1970's and used for the first Mars Lander mission, Viking [1]. The development of this parachute consisted of wind tunnel testing [2], [3], [4], low-altitude drop testing [5], and high altitude supersonic parachute testing [6], [7], [8]. After the success of the twin Viking landers, all subsequent NASA Mars landing missions have used a variant of this supersonic DGB parachute design. These missions include Mars Pathfinder (1997) [9], [10], Mars Exploration Rovers (2004) [11], Phoenix lander (2007) [12], Mars Science Laboratory (2012) [13], and the InSight Lander (2018). For each of these missions, the parachute was sized for the given payload and modified in response to technological improvements, but otherwise largely maintained the same characteristics of the original DGB parachute design. Additionally, after Viking, parachute development and qualification testing was limited to subsonic testing via low-altitude drop tests or wind tunnel tests. These tests were generally thought to be structural qualification tests under a hypothesis that the parachute stresses and loads seen during supersonic inflation could be adequately replicated in a subsonic inflation.

In 2014 & 2015 the Low-Density Supersonic Decelerators (LDSD) project tested multiple large aerodynamic decelerator technologies that could be used at Mars including two variants of a 30.5 meter diameter supersonic parachute [14], [15]. While other aerodynamic decelerator technologies performed nominally, the parachutes used in these flight tests failed during inflation [14], [16]. Furthermore, the parachute design that failed in each test had been tested subsonically and shown to survive loads higher than those seen in supersonic flight. This led to a critical need to better understand the dynamics of a supersonic parachute inflation in a Mars-like environment. The Advanced Supersonic Parachute Inflation Research Experiments (ASPIRE) project was formed in order to develop a method of testing full-scale parachutes for Mars at supersonic speeds in conditions that are analogous to those of a Martian entry.

The primary objective of ASPIRE was to act as a risk reduction test activity for the Mars 2020 supersonic parachute [17]. Two candidate parachutes for the Mars 2020 mission were tested across three flights between October 2017 and September 2018. The first candidate parachute was a Build-to-Print version of the Mars Science Laboratory (MSL) parachute built by Pioneer Aerospace. The second parachute was a Strengthened DGB parachute that had the same geometry but differed in materials and construction and was built by Airborne Systems.

ASPIRE used a two stage Terrier-Black Brant IX sounding rocket launched out of Wallops Flight Facility (WFF) in Virginia to deliver these parachutes to Mars-relevant Mach numbers and dynamic pressures. ASPIRE was focused on understanding the inflation process and structurally testing the candidate M2020 parachutes, so each ASPIRE flight targeted a peak inflation load and corresponding dynamic pressure. The first ASPIRE flight, designated SR01, occurred on October 4th, 2017 and carried the MSL Build-to-Print Chute while the second (SR02) and third (SR03) flights tested the Strengthened Parachute design.

B. Paper Organization

This paper will present an overview of all three ASPIRE flights. First, the Test Architecture that was used for all three ASPIRE flights will be presented. This will be broken down into an explanation of the Concept of Operations, the parachute test articles, and the data sources and processes used to reconstruct the flight trajectories and parachute performance. Then the mission operations will be summarized, focusing on critical differences between the flights. Next, the high level results along with brief analysis for all three ASPIRE flights will be presented. Lastly this paper will discuss the conclusions from those results.

III. ASPIRE Test Architecture

Each ASPIRE payload was rail launched atop a 2 stage Terrier-Black Brant IX sounding rocket. Figure 1 shows the length of the vehicle and a breakdown of each payload subsystem. This vehicle and payload configuration was consistent across all three ASPIRE flights.

A. CONOPS

Figure 2 shows the general Concept of Operations (CONOPS) for all three ASPIRE flights. Note that the conditions at each event are approximate and varied with each flight as the targeted test condition was adjusted. The vehicle is rail

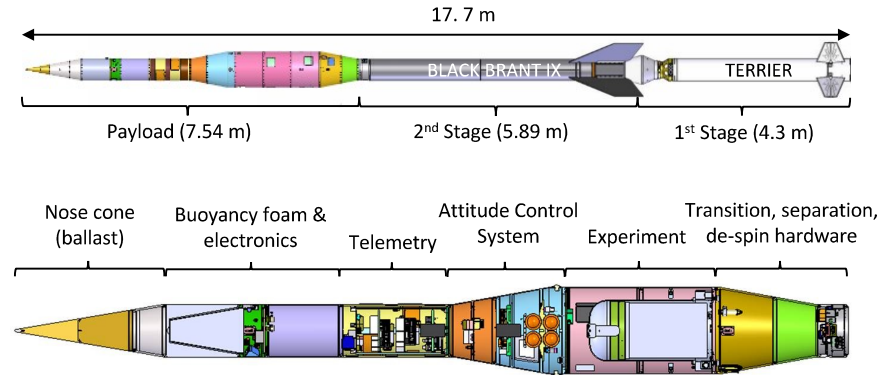


Fig. 1 ASPIRE Payload Configuration

launched from the 50K launcher on Wallops Island, Virginia. The first stage Terrier motor burns for approximately 6 seconds while the vehicle is spun up for stabilization using spin motors. The second stage Black Brant IX then ignites for an approximately 25 second burn, concluding with the vehicle achieving roughly Mach 3.3 at second stage burnout. About 60-70 seconds later, the payload then performs a yo-yo despin maneuver to null the roll rate and separates from the Black Brant. The payload is then in the coast phase where cold gas thrusters null any residual rates leading up to parachute deploy. After coasting through an apogee of 45-55 km, the parachute is then mortar deployed when the onboard computer calculates that the payload has achieved the target dynamic pressure condition. Within 2 seconds of mortar fire the parachute is fully inflated and within 6 seconds has decelerated to subsonic speeds. The payload and parachute descend toward the Atlantic Ocean and a heavily ballasted nosecone separates from the vehicle at an altitude of about 3 km so that the payload will remain buoyant in the water. About 30 minutes after launch, the ASPIRE payload splashes down and a recovery crew recovers both the parachute and payload.

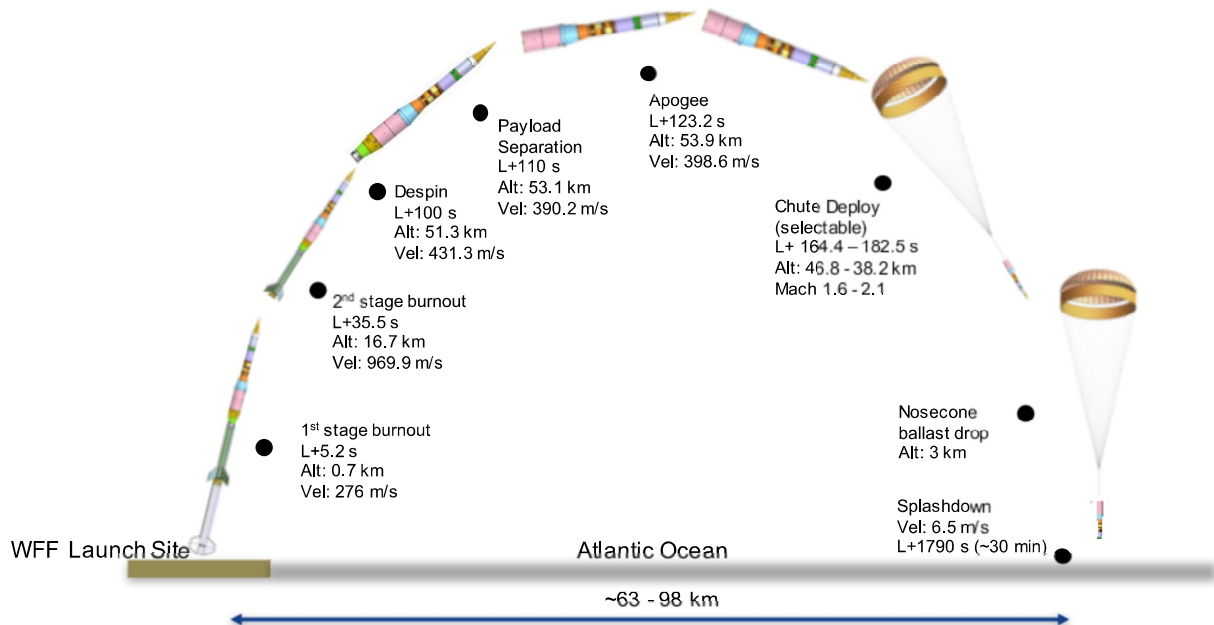


Fig. 2 ASPIRE General Concept of Operations

B. Test Article Description

The MSL Build-to-Print Chute, flown on SR01, was a 21.5 meter D_0 DGB parachute made of Nylon, Technora, and Kevlar with a parachute assembly mass of ~58 kg. This parachute design was used successfully for the MSL mission when it landed on the surface of Mars in August of 2012 [13]. The Strengthened parachute, flown on SR02 and SR03, has the same basic geometry but utilized stronger materials and modifications in construction techniques. The Strengthened parachute had an assembly mass of ~88 kg. Both designs are geometrically scaled versions of the DGB design initially by the Viking missions to Mars. More details about the ASPIRE parachute test articles are presented in References [17] and [18].

C. Data Sources

The ASPIRE payload was equipped with instrumentation to measure the trajectory, aerodynamics, and performance of the test vehicle and test article. Additional instrumentation was used to provide diagnostic information on the payload and its electrical systems, such as temperature or voltage information. A summary of the primary on-board instrumentation is provided in Table 1.

Table 1 Key Test Vehicle Instrumentation Summary

Device	Make & Model	Rate	Resolution	Location*
Primary IMU	GLN-MAC (LN-200)	400 Hz	NA	ACS section
Experimental IMU	NSROC Tern INS	400 Hz	NA	Telemetry section
GPS	Javad TR-G2	20 Hz	NA	Telemetry section
Load pins (x3)	Strainert custom	1 kHz	1100 lbf [†]	Experiment section
HS Cameras (x3)	IDT OSX	1000 fps	3840x2400	Experiment section
Situational Video (x3)	GoPro Hero4	120 fps [‡]	1920x1080 [‡]	Experiment section

* See Figure 1.

[†] Estimated 3σ uncertainty of total parachute force for SR01 and SR02. For SR03, it was ~1700 lbf. 90 klbf capability, each pin calibrated to 25 klbf on SR01 & SR02 and 40 klbf on SR03.

[‡] Only 2 cameras used on SR01; one camera recorded at 30 fps and 4K resolution for SR02 and SR03

The test vehicle included a C-band radar beacon with two diametrically opposed antennas located on the section of the payload containing the buoyancy foam (see Figure 1). Multiple fixed radars on the WFF range were used to track the vehicle.

Atmospheric characterization was achieved using a number of meteorological balloons carrying LMS-6 radiosondes. Up to six balloons were launched for each opportunity to provide information on the winds, temperature, and humidity at altitudes of up to approximately 40 km. Pressure and density were subsequently derived using temperature versus altitude data and assuming the atmosphere was in hydrostatic equilibrium. At altitudes above those achieved by the balloons, atmospheric states were obtained from the Goddard Earth-Observing System, Version 5 (GEOS-5). Details of the atmospheric reconstruction during each flight, including instrumentation and results are provided in References [18] and [19].

After synchronization, the various data sources were incorporated into the reconstruction process. The trajectory of the payload was reconstructed using NewSTEP, a dual-pass Extended Kalman Filter (EKF) developed at NASA LaRC [20]. The filter incorporates the data from the NIACS, GPS, radar, and meteorological instrumentation as well as information about the vehicle configuration to reconstruct the trajectory of the payload from launch until loss of telemetry signal.

IV. Mission Ops

Table 2 summarizes the reconstructed flight event conditions for all three flights. This table can be used as a reference when results and analysis are presented elsewhere in this paper. Example images of launch and descent are provided in Figure 3.

The first ASPIRE flight (SR01) took place on October 4th, 2017, the second (SR02) on March 31st 2018, and the third (SR03) on September 7th 2018. Launch took place at 06:45 EDT, 12:19 EDT, and 09:30 EDT for SR01, SR02, and SR03 respectively. SR01 and SR03 were able to launch at the beginning of their planned launch window while SR02 was delayed. With an original opening of the launch window at 10:00 EDT for SR02, high winds at the range that day led to non-ideal sea states which would have hindered recovery operations. Later in the day the winds had decreased enough to allow for launch at 12:19 EDT.

All three vehicles exited the launch rail nominally before being spin-stabilized at ~ 4 Hz by motors on the 1st stage. After 1st stage burnout, the second stage ignited for a ~ 25 second burn before coasting to payload separation about 104 seconds into the flight. Prior to payload separation the de-spin maneuver was able to reduce the roll rates enough for the active attitude control (NIACS) to null any residual rates on all three flights. At separation the payload was traveling at a wind relative velocity of about 400 m/s. For SR01 the conditions at separation lined up with pre-flight predictions which led to nominal test conditions. SR02 on the other hand exhibited a 3σ high velocity and altitude compared to pre-flight predictions for payload separation. This had an impact on the test conditions for this flight, namely the Mach number (to be presented in the next section). For the 3rd flight the launch vehicle thrust and drag model was updated in order to better predict its performance. Due to this change on SR03 the separation conditions were once again comparable to pre-flight predictions.

After payload separation the vehicle coasted to apogees of 51 km, 55 km, and 49 km on SR01, SR02, and SR03 respectively. During this phase of flight, the NIACS maintained nominal attitude and roll rates for the vehicle and kept the total angle of attack less than 2 deg leading up to parachute deploy. When the onboard computer detected that the test conditions were met, a trigger was initiated which started a sequence of events that initiated instrumentation before mortar fire about 1 second after trigger. The reconstructed dynamic pressure at the trigger condition was within 6% of preflight predictions for all three flights. The test conditions for each flight are summarized in Table 2. Each parachute maintained structural integrity throughout deployment and inflation and reached subsonic conditions within 6 seconds of mortar fire. After reaching a stable descent condition the payload separated the nosecone ballast at an altitude of 3 km before splashing down about 30 minutes into the flight.

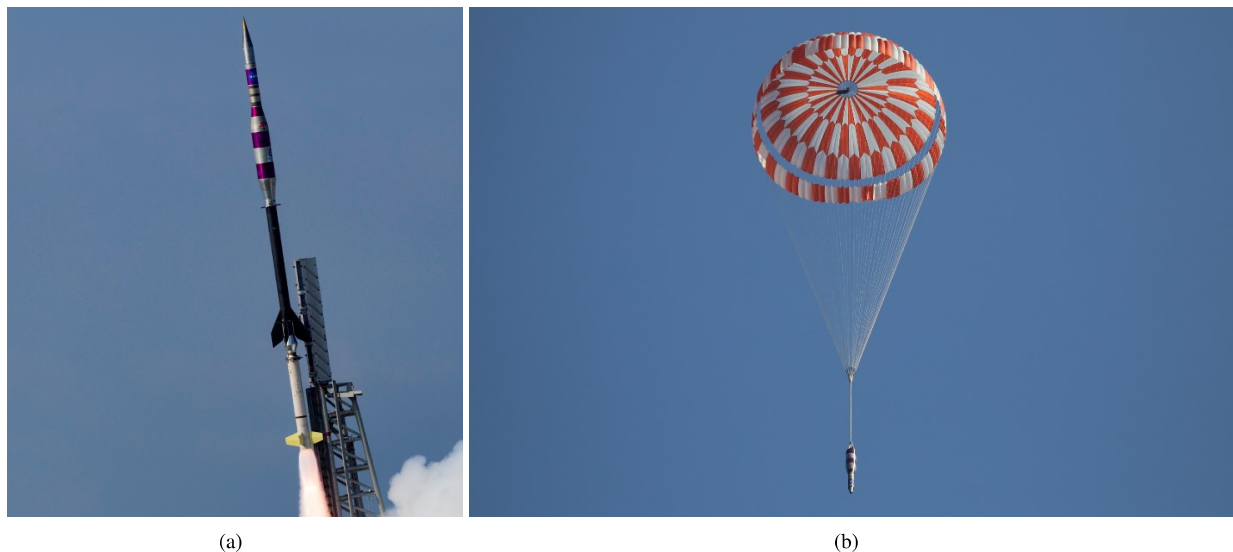


Fig. 3 ASPIRE SR03 vehicle on the launch rail and during descent

For the first and third ASPIRE flights (SR01 & SR03) the recovery crew was able to spot the payload and witness splashdown from about 100 yards away. For these flights the parachute and payload recovery operation was carried out seamlessly. On SR02 both the windy conditions and the over performance of the launch vehicle caused splashdown to occur a few miles away from where the recovery vessels were positioned. The payload and parachute were found about 45 minutes after splashdown, but not before the parachute had been fully submerged about 40 meters below the payload. In the end the parachute and payload were recovered successfully with no significant damage to either. Figure 4 shows the state of the payload and parachute upon arrival. All onboard data was successfully recovered for all three flights.

Table 2 ASPIRE Event Conditions

Event	T+ sec	Mach	Dyn Pres Pa	WR Vel m/sec	Altitude km	FPA deg	Total AoA deg
SR01							
Launch	0.00	0.01	8.3	3.7	-0.02	35.7	61.7
Payload Separation	104.03	1.27	87.2	407.8	49.92	20.6	5.9
Apogee	119.05	1.19	65.7	379.7	51.00	0.0	2.1
Mortar Fire	161.41	1.77	452.4	560.3	42.40	-46.4	0.5
Line Stretch	162.37	1.79	491.7	567.7	42.01	-47.1	1.0
Peak Load	162.88	1.77	494.7	560.9	41.80	-47.4	0.9
2nd Peak Load	163.09	1.71	466.3	541.3	41.71	-47.6	2.0
Mach 1.4	164.36	1.40	332.1	441.9	41.25	-48.9	5.5
Mach 1.0	167.02	1.00	188.1	314.7	40.49	-53.0	5.8
Nose Cone Jettison	1554	0.03	44.9	10.0	3.02	-85.0	7.7
Splashdown	2061	0.02	30.5	6.9	-0.01	-51.1	39.6
SR02							
Launch	0.00	0.02	33.3	7.2	-0.03	5.7	84.9
Payload Separation	103.99	1.24	53.8	398.1	53.00	28.0	3.8
Apogee	123.49	1.10	33.6	353.3	54.82	0.0	3.0
Mortar Fire	177.59	1.97	670.6	626.8	40.77	-55.8	4.3
Line Stretch	178.63	2.00	744.6	636.4	40.27	-56.2	1.9
Peak Load	179.08	1.97	746.5	626.1	40.03	-56.4	0.6
2nd Peak Load	179.27	1.89	694.7	600.0	39.93	-56.4	5.0
Mach 1.4	180.72	1.40	416.5	444.3	39.31	-56.9	15.9
Mach 1.0	182.86	1.00	233.1	316.1	38.63	-59.4	2.8
Nose Cone Jettison	1568	0.03	31.4	8.2	2.93	-72.7	8.5
Splashdown	2030	0.02	41.4	7.8	0.02	-49.3	45.3
SR03							
Launch	0.00	0.03	59.4	10.0	-0.04	-5.0	86.0
Payload Separation	104.06	1.17	96.4	372.5	48.10	18.7	0.1
Apogee	116.53	1.11	79.4	354.8	48.85	0.0	2.7
Mortar Fire	163.82	1.85	931.7	575.8	38.12	-51.9	0.2
Line Stretch	164.85	1.88	1028.4	584.7	37.65	-52.5	0.9
Peak Load	165.26	1.85	1020.1	573.2	37.45	-52.8	0.5
2nd Peak Load	165.46	1.73	909.6	537.6	37.37	-52.9	1.1
Mach 1.4	166.15	1.40	615.5	434.5	37.10	-53.9	8.0
Mach 1.0	167.59	1.00	333.6	311.6	36.67	-55.8	6.2
Nose Cone Jettison	1486	0.03	48.5	10.5	3.15	-78.9	18.6
Splashdown	1982	0.02	35.0	7.8	0.00	-69.8	22.4



Fig. 4 Recovery vessel arriving at payload and parachute after splashdown

After each ASPIRE flight the parachute was rinsed free of salt water then hung to dry for a few days before being shipped out to US Naval Weapons Center China Lake for a detailed inspection.

More details about the mission operations for all three ASPIRE flights can be found in References [18], [19].

V. Test Results

A. Atmosphere and Test Conditions

On the day of launch, between four and six 3000 g high-altitude balloons carrying radiosondes were released at regular intervals. These allowed the reconstruction of the atmospheric state up to approximately 40 km. Above this altitude, the atmospheric profile was obtained from GEOS-5. The resultant atmospheric profiles were used to reconstruct the atmosphere-relative state throughout the three trajectories. The wind-relative dynamic pressure, payload velocity, Mach number, total angle of attack, and flight path angle are shown at key events in Table 2.

B. Parachute Deployment and Inflation

All three ASPIRE parachutes were packed and mortar deployed in a manner similar to how they would be for Mars flight. Each ASPIRE flight sought to characterize four events associated with deployment and inflation: mortar fire (MF), line stretch (LS), bag strip (BS), and full inflation (FI). The timing of line stretch was determined based on the initial rise in loads measured as the canopy begins emerging from the parachute pack. The timing of parachute full inflation is here defined as when the first peak load is measured.

For all three ASPIRE flights, parachute deployment occurred without any significant issues. The mortar velocities achieved were all within expectations based on ground testing and the packs proceeded to line stretch without any entanglement or dumping of the suspension lines. Some differences in pack rotation were observed. For SR01, line stretch was achieved with the pack largely parallel to the direction of motion, while on SR02, the pack was rotated to approximately 170 degrees, with the top of the bag visible at the time of line stretch. For SR03, the pack was roughly sideways to the direction of motion at the time of line stretch. Initially the amount of pack rotation seen in SR02 was surprising, but upon review of deployment videos from prior supersonic and subsonic parachute tests, large amounts of pack rotation was noted to be common.

Although the bag strip process was largely obscured by the inflating parachutes, some assessments of estimated bag strip times were made based on calculated velocities at line stretch. In the case of SR03, the bag was visible through the vent of the inflating parachute at least 53 ms sooner than was predicted based on the bag velocity at line stretch. This was noted as likely being due to the canopy inflating faster than the bag could come off of the parachute, effectively having the parachute pull itself out of the bag. This also resulted in the momentum of the bag being decreased to the point where the bag did not invert after bag strip, as evidenced by imagery showing the outer portion of the bag being visible through the parachute vent.

A sequence of images for each of the three inflation events is provided in Figure 5 and inflation times are provided in Table 3. Inflation for all three parachutes occurred without any major entanglement or snags. In each case, the band was observed to emerge from the pack coincident with the timing of line stretch and it proceeded to inflate radially outwards. Inflation of the band was followed by the exposure of the disk and rapid pressurization of that portion of the canopy. For SR01, the geometry appeared to develop in a remarkably symmetric manner while for SR02 and SR03, more asymmetry was evident in the very early portions of inflation, but later gave way to a more symmetric projected

geometry. Inflations faster than the 0.635 seconds of the MSL canopy [21] were expected for the ASPIRE flights due to the increased speed of sound at Earth and higher test velocities. However, each subsequent flight resulted in faster inflations and it is hypothesized that there is likely a weak dependence on dynamic pressure with inflation time.

Figure 6 shows the load trace of the parachute force (F_{chute}) for each flight, synchronized at the time of line stretch. Note that the parachute force here is defined as not the tension measured by the load pins, but the total aerodynamic force generated by the parachute which includes the inertial load of the parachute itself (i.e. the product of the mass of the parachute system and the measured deceleration at full inflation). All three flights showed a characteristic rapid rise to an initial peak force, subsequent decrease in load, and a rebound to a 2nd peak of similar, or in the case of SR02, larger load. Oscillations following the 2nd peak were relatively minor and close in frequency to the elastic mode of the suspension system. The dip in load on SR02 at approximately 1.2 seconds after line stretch was associated with the parachute traversing the wake of the payload.

The high speed imagery allowed for a reconstruction of the parachute projected area [22], and those results are shown in Figure 7 along with a normalized load trace. Of note is that the 1st peak in measured load consistently preceded the initial peak in projected area. Furthermore, the decrease in load was also larger in percentage than the corresponding decrease in projected area, indicating that the canopy was depressurizing as well.

An initial inspection of each parachute was performed after recovery and a more detailed inspection later by the Escape, Parachute and Crashworthy Division at China Lake. For each flight minor damage was observed in the parachute that was dispositioned as being related to the deployment process. Although none of the damage was considered to be large enough to be of concern, some minor changes were made in the parachute bag design and how it is retained by the parachute after deployment.

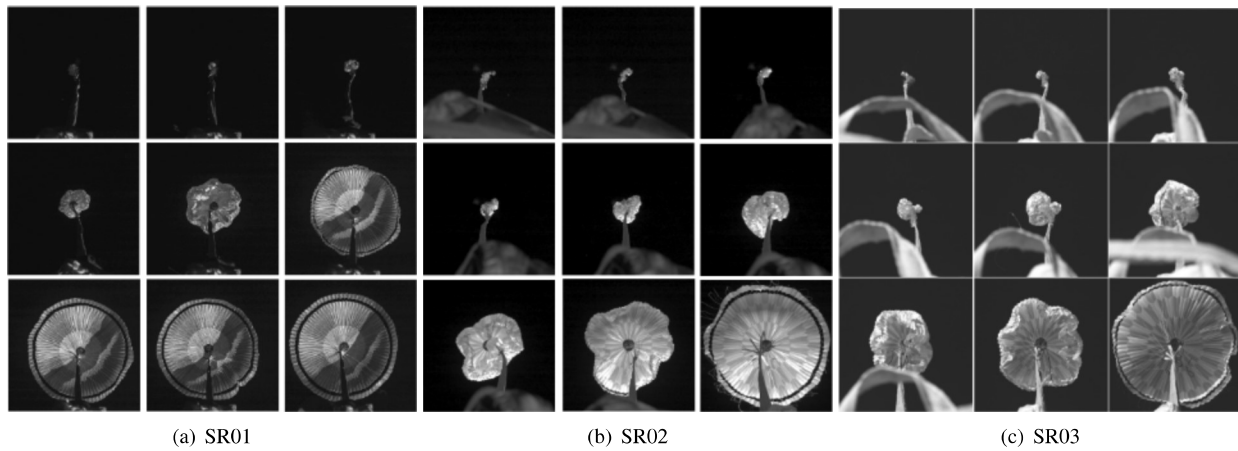


Fig. 5 High Speed Camera Images from Line Stretch to Mortar Fire (Note: images are not at evenly spaced times)

Table 3 Parachute Inflation Results

Parameter	Units	SR01	SR02	SR03
Time from MF to LS	sec	0.961	1.038	1.027
Time from LS to FI	sec	0.506	0.456	0.410
F_{chute} @ Full Inflation	lbf	32,387	50,491	67,369
F_{chute} @ 2nd peak	lbf	32,336	55,949	66,515
q_{∞} @ Full Inflation	Pa	494.7	746.5	1020.1
Mach @ Full Inflation		1.77	1.97	1.85
D_0 , as-built	m	21.31	21.51	21.55
S_0 , as-built	m ²	356.80	363.34	364.62

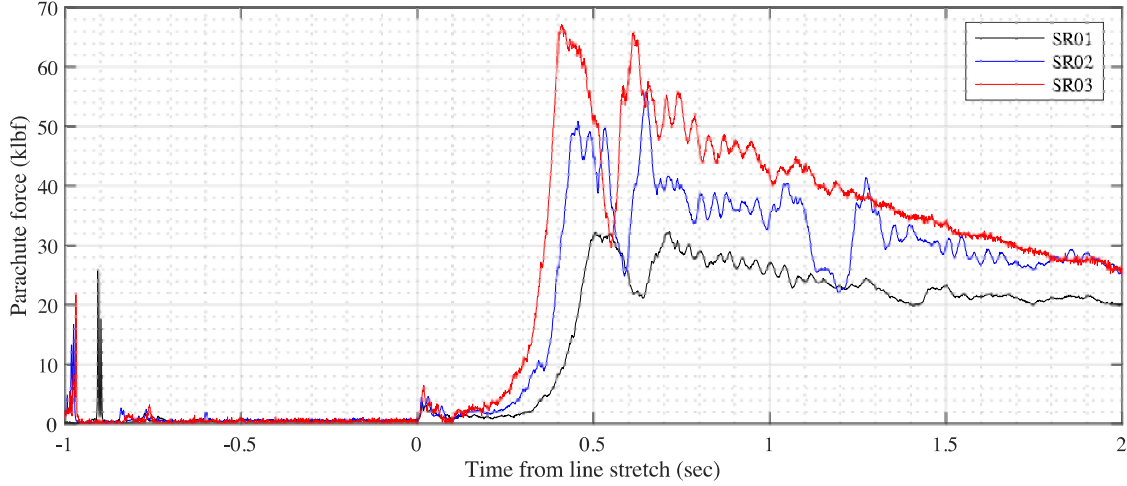


Fig. 6 Measured parachute force during inflation

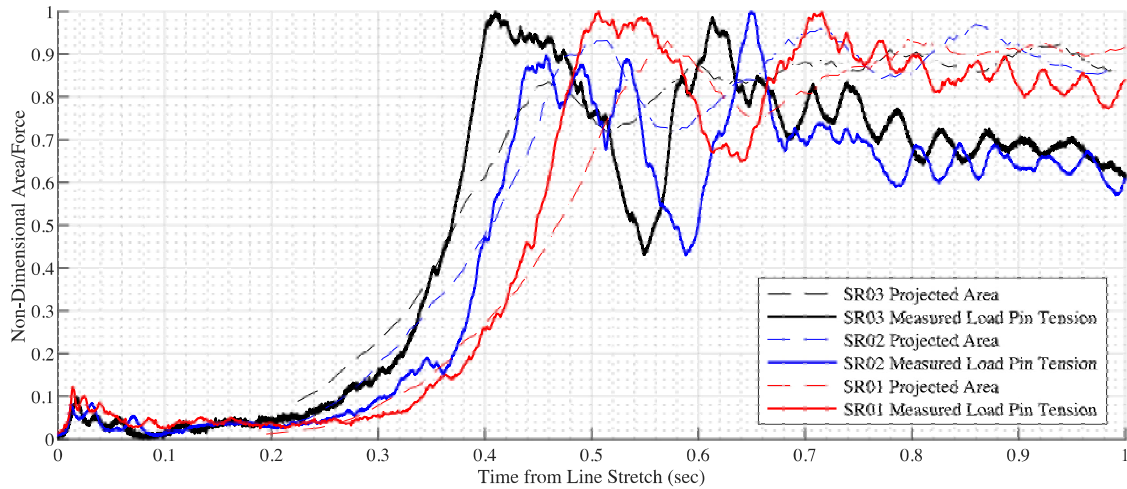


Fig. 7 Normalized parachute loads in projected areas vs. time from line stretch

C. Parachute and Payload Dynamics

Figure 8(a) shows the reconstructed parachute drag coefficient (C_D) as a function of Mach number for SR01, SR02, and SR03. The force exerted by the parachute on the payload was calculated by two independent methods: from the triple bridle load pin measurements and from the NIACS accelerometer data. Only the accelerometer results are shown in Figure 8 as the results from both methods were in excellent agreement and the load pins were not sized to record the small parachute forces during terminal descent [18, 19]. The parachute drag force (F_D) was calculated by projecting the parachute force vector onto the wind-relative anti-velocity vector, and a parachute drag coefficient was computed as:

$$C_D = \frac{F_D}{q_\infty S_0} \quad (1)$$

where q_∞ is the freestream dynamic pressure, and S_0 is the parachute reference area. The solid black, blue, and red lines in Figure 8 denote a rolling average of the reconstructed C_D from the NIACS measurements as a function of Mach number for SR01, SR02 and SR03, respectively. The averaging was performed over all values of C_D in sliding bins of width $\text{Mach} = 0.03$. The pre-flight model for the parachute drag coefficient, which was a function of the Mach number only, is also shown for reference. The solid green line indicates the nominal values of C_D as a function of Mach number in the pre-flight model, while the dashed green lines indicate the pre-flight upper and lower bounds on

C_D . The reconstructed parachute total force coefficient (C_{tot}) from MSL [21] is also shown for comparison. Detailed comparisons of inflations behind a slender vs. blunt body are presented in Reference [24].

At all Mach numbers, the results from SR01 through SR03 were in excellent agreement with each other. In addition, the results from the three flights were in excellent agreement with the pre-flight parachute drag model at Mach numbers below 0.75. Above Mach 0.75, however, the reconstructed C_D differed from the pre-flight model in two key ways. First, the reconstructed C_D above Mach 1.1 was generally lower than the nominal pre-flight estimate. Second, between Mach 0.8 and 0.9, the reconstructed drag coefficient increased steadily from the average subsonic value to an average supersonic value of approximately 0.72 in all three flights. This change in drag with Mach number occurred at a lower Mach number than predicted based on previous DGB flights (cf. the MSL parachute total force coefficient). The lower Mach onset of the C_D decrease is potentially a consequence of testing in the wake of a slender body [23]. Figure 8(b) shows the post-flight drag model developed in response to these differences. The development of this model is described in detail in Reference [23].

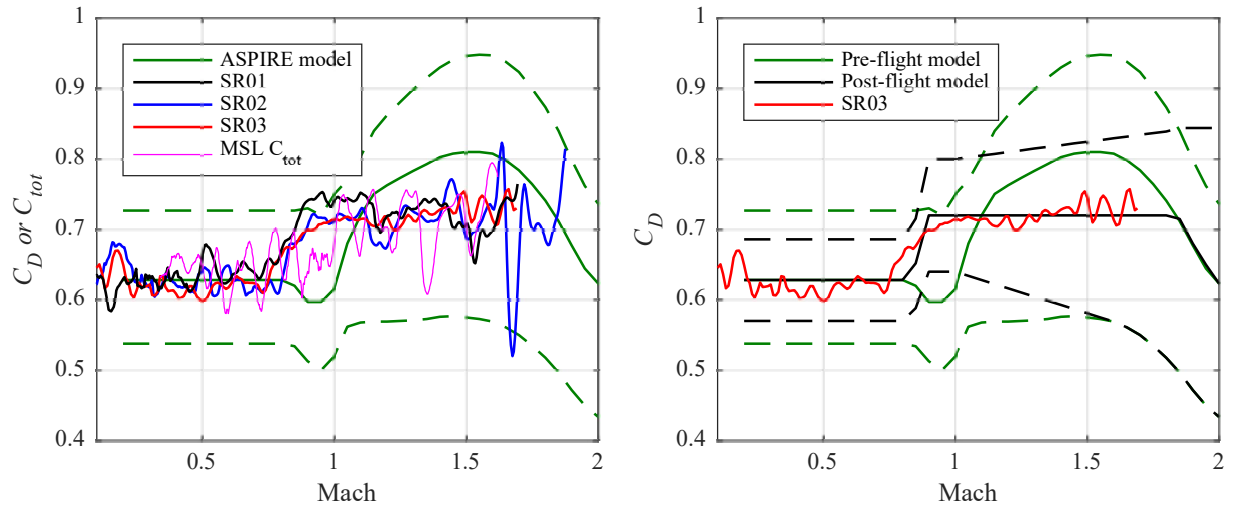


Fig. 8 Rolling average of the reconstructed parachute C_D from 0.5 sec after full inflation until subsonic terminal descent. The averaging was performed over all values of C_D in sliding bins of width Mach = 0.03. The results for all three ASPIRE flights are shown in (a), along with the reconstructed C_{tot} from MSL and the pre-flight drag model. In (b) the post-flight drag model is compared against the pre-flight model, with the results from SR03 included for reference.

In Figure 8, the reconstructed C_D for SR02 showed significantly greater oscillations above Mach 1.5 than the other two flights. As discussed in Section V.B, parachute deployment and inflation occurred at a higher Mach number on SR02. Following inflation, the parachute and payload exhibited more significant dynamics than in the other two flights. In Figure 9 which shows the parachute pull angle (the angle between the parachute force vector and the vehicle centerline), it is evident that the parachute experienced more motion relative to the payload in the second flight. By assuming that the parachute axis of symmetry was approximately aligned with the parachute force vector and that the canopy vent remained at a fixed trailing distance from the payload, the approximate motion of the vent relative to the payload was calculated and is shown in Figure 10.

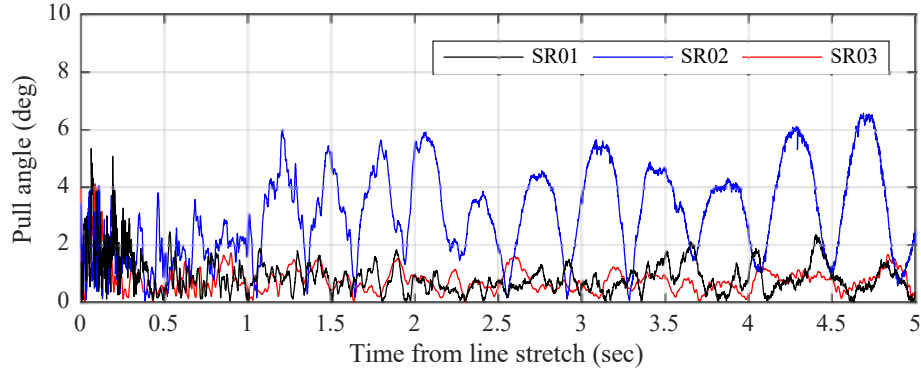


Fig. 9 Time histories of the parachute force pull angle during the first five seconds after line stretch.

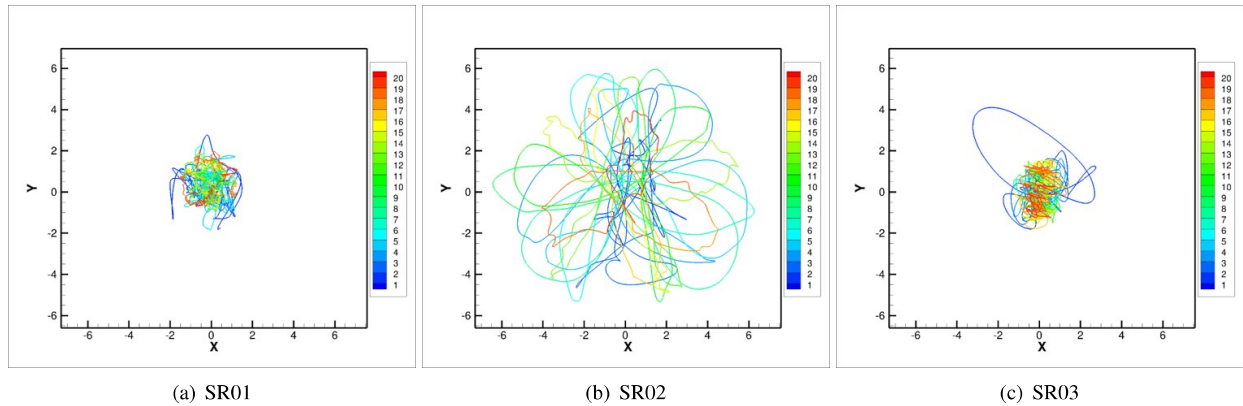


Fig. 10 Parachute vent position relative to payload centerline from mortar fire to 20 sec after mortar fire. The horizontal and vertical axes represent the vent position in a frame fixed to the payload (in meters). The color bar shows the time elapsed since mortar fire (in seconds).

The increased motion of the parachute relative to the payload in SR02 resulted in greater dynamics being imparted to the payload. Figure 11(a) shows the root-sum-square (RSS) of the lateral angular rates measured by the NIACS during the first 50 sec following mortar fire. On SR02, the lateral rates peaked at 87.7 deg/s, more than twice the peak lateral rates on SR01 and SR03 during the same period. Figure 11(b) shows the payload roll rate during the same period. During inflation, asymmetric loading of the parachute bridle induced a rolling torque on the payload. Due to the small inertia of the payload about its roll axis (less than 50 kg-m²), the payload experienced significant roll rates following inflation on all three flights. On SR02, these rates reached 180 deg/s owing to the large parachute pull angles. In all three flights, the direction of roll was reversed starting between 15 sec and 20 sec after mortar fire. This reversal was caused by the parachute riser twisting on itself and beginning to act as a torsional spring. The winding and unwinding of the riser as the payload spun about its roll axis continued throughout the entire descent on all three flights.

Time histories of the payload wind-relative total angle of attack during the first 50 sec of the parachute phase are shown in Figure 11(c). In the three flights, the total angle of attack began increasing immediately after full inflation. The increase in the total angle of attack continued until 6 to 8 sec after mortar fire, when it achieved a mean value of about 15 deg and continued to oscillate about this value. Throughout this period, the angles of attack and sideslip oscillated owing to the rotation of the payload about its rolls axis.

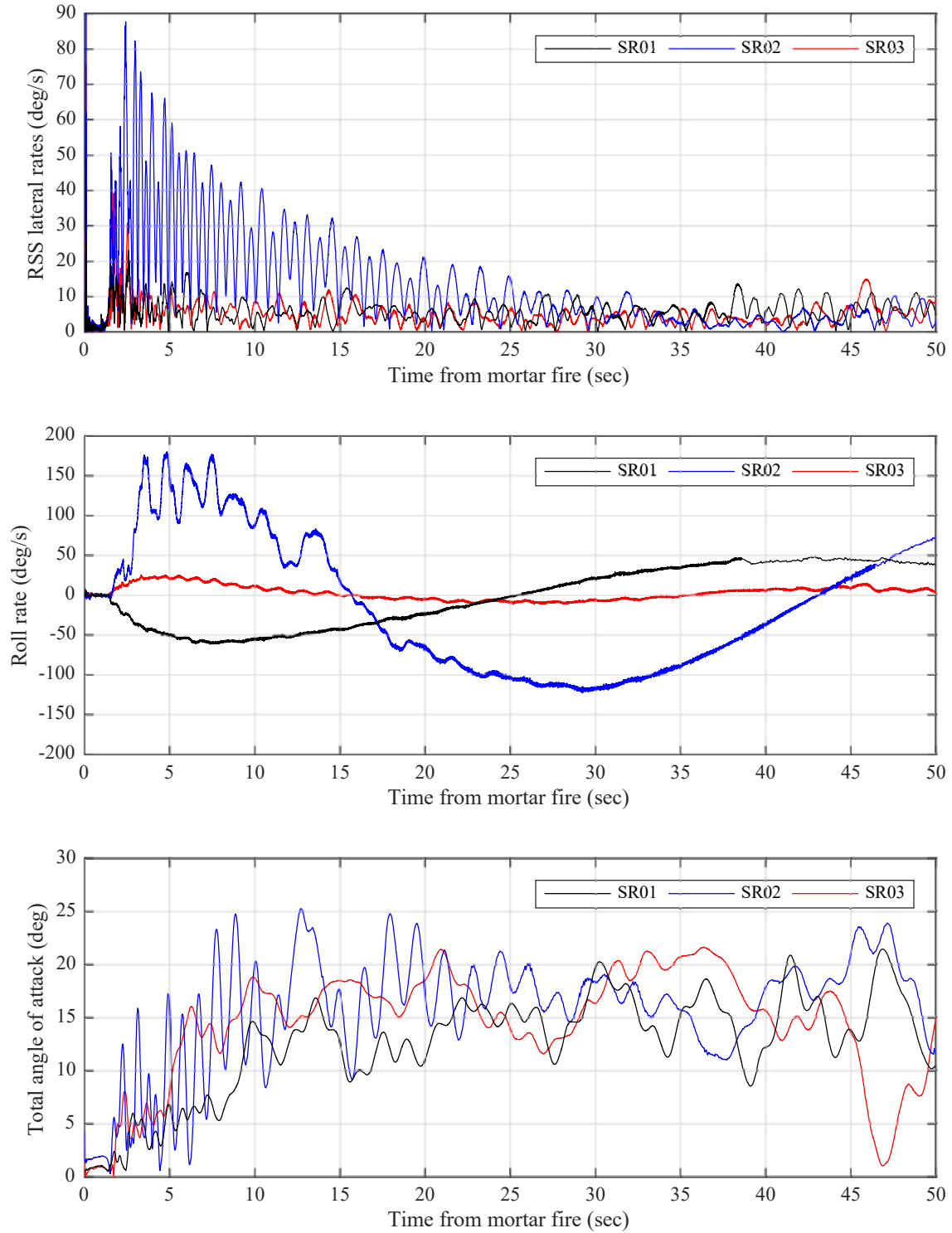


Fig. 11 Payload (a) lateral rates (RSS), (b) roll rate, and (c) total angle of attack during the first 50 sec of the parachute phase for SR01-SR03.

VI. Conclusions and Lessons Learned

Two candidate parachute designs for the Mars 2020 mission were tested at Mars-relevant conditions across 3 flights between October 2017 and September 2018. For all three flights the parachute was delivered to the desired test conditions and all data necessary to reconstruct parachute performance was recorded and recovered successfully. The parachutes were deployed at dynamic pressures ranging from 452 to 932 Pa and Mach numbers between 1.77 and 1.97. The parachutes exhibited a peak force of 32.4, 55.9, and 67.4 klbf on the first, second, and third flights respectively. Across all three ASPIRE flights both candidate parachutes performed nominally. Despite the varying activity observed between the three flights, such as the dynamic movement of the parachute in SR02 or the parachute inflating out of its bag on SR03, the parachutes withstood the stresses of deployment and inflation without significant damage. On SR03 the Strengthened chute even experienced a load that is 40% higher than the highest load expected for the Mars 2020 mission.

The ASPIRE project successfully completed its primary objective of reducing risk for the Mars 2020 mission. Other than the parachutes withstanding the supersonic inflation, there were other lessons learned about this deployment and inflation environment throughout this test campaign. Those included lessons in parachute bag dynamics prior to line stretch, parachute inflation times, and parachute aerodynamics. For the latter, an updated C_D vs. Mach number relationship was developed for supersonic inflation behind a slender body such as the ASPIRE payload. The resulting coefficient of drag was consistent across all three ASPIRE flights but differed from the MSL total force coefficient.

The ASPIRE project successfully developed an architecture that can be used to test full scale parachutes for Mars landing missions. The ability to replicate the conditions for a supersonic parachute inflation at Mars has proven invaluable for current and future Mars missions. The data acquired from the three ASPIRE flights has been crucial for certifying the parachute for flight on Mars 2020 and will further serve to augment the understanding of supersonic parachute inflations.

Acknowledgments

This research was carried out at the Jet Propulsion Laboratory, California Institute of Technology, under contract with the National Aeronautics and Space Administration. The authors would like to gratefully acknowledge the many contributions of the members of the ASPIRE team from Wallops Flight Facility, NASA Langley Research Center, NASA Ames Research Center, and Jet Propulsion Laboratory.

References

- [1] Cooley, C. G., and Lewis, J. G., "Viking 75 Project: Viking, Lander System Primary Mission Performance Report," *NASA Contractor Report*, , No. CR-145148, April 1977.
- [2] Galigher, L. L., "Aerodynamic Characteristics of Ballutes and Disk-Gap-Band Parachutes at Mach Numbers from 1.8 to 3.7," *AEDC Technical Report*, , No. AEDC-TR-69-245, Nov 1969.
- [3] Bobbitt, P. J., Mayhue, R. J., Faurote, G. L., and Galigher, L. L., "Supersonic and Subsonic Wind-Tunnel Tests of Reefed and Unreefed Disk-Gap-Band Parachutes," *AIAA Paper*, , No. 1970-1172, Sept 1970.
- [4] Jaremenko, L., Steinberg, S., and Faye-Petersen, R., "Scale Model Test Results of the Viking Parachute System at Mach Numbers from 0.1 Through 2.6," *NASA Contractor Report*, , No. CR-149377, 1971.
- [5] Eckstrom, C. V., and Murrow, H. N., "Flight Tests of Cross, Modified Ringsail, and Disk-Gap-Band Parachutes from a Deployment Altitude of 3.05 km (10,000 ft)," *NASA Technical Memorandum*, , No. TM X-2221, June 1971.
- [6] Eckstrom, C. V., and Preisser, J. S., "Flight Test of a 30-Foot-Nominal-Diameter Disk-Gap-Band Parachute Deployed at a Mach Number of 1.56 and a Dynamic Pressure of 11.4 Pounds Per Square Foot," *NASA Technical Memorandum*, , No. TM X-1451, Aug 1967.
- [7] Preisser, J. S., and Eckstrom, C. V., "Flight Test of a 40-Foot-Nominal-Diameter Disk-Gap-Band Parachute Deployed at a Mach Number of 1.91 and a Dynamic Pressure of 11.6 Pounds Per Square Foot," *NASA Technical Memorandum*, , No. TM X-1575, Aug 1968.
- [8] Preisser, J. S., and Eckstrom, C. V., "High Altitude Flight Test of a Reefed 12.2-Meter Diameter Disk-Gap-Band Parachute With Deployment at a Mach Number of 2.58," *NASA Technical Memorandum*, , No. TN D-6469, Aug 1971.

- [9] Fallon, E. J., "System Design Overview of the Mars Pathfinder Parachute Decelerator Subsystem," *AIAA Paper*, , No. 1997-1511, 1997.
- [10] Spencer, D. A., Blanchard, R., Braun, R. D., Kallemeyn, P. H., and Thurman, S. W., "Mars Pathfinder Entry, Descent, and Landing Reconstruction," *Journal of Spacecraft and Rockets*, Vol. 36, No. 3, 1999, pp. 357–365.
- [11] Witkowski, A., and Bruno, R., "Mars Exploration Rover Parachute Decelerator System Program Overview," *AIAA Paper*, , No. 2003-2100, 2003.
- [12] Adams, D. S., Witkowski, A., and Kandis, M., "Phoenix Mars Scout Parachute Flight Behavior and Observations," *IEEE Aerospace Conference Paper*, , No. 1534, 2011.
- [13] Cruz, J. R., Way, D. W., Shidner, J. D., Davis, J. L., Adams, D. S., and Kipp, D. S., "Reconstruction of the Mars Science Laboratory Performance and Comparison to the Descent Simulation," *AIAA Paper*, , No. 2013-1250, 2013.
- [14] Clark, I., and Adler, M., "Summary of the Second High-Altitude, Supersonic Flight Dynamics Test for the LDSD Project," *IEEE Aerospace Conference Paper*, March 2016.
- [15] Gallon, J., Witkowski, A., Clark, I. G., Rivellini, T., and Adams, D. S., "Low Density Supersonic Decelerator Parachute Decelerator System," *AIAA Aerodynamic Decelerator Systems (ADS) Conference*, 2013, p. 1329.
- [16] Clark, I. G., Manning, R., and Adler, M., "Summary of the First High-Altitude, Supersonic Flight Dynamics Test for the Low-Density Supersonic Decelerator Project," *23rd AIAA Aerodynamic Decelerator Systems Technology Conference*, 2015.
- [17] Tanner, C. L., Clark, I. G., and Chen, A., "Overview of the Mars 2020 Parachute Risk Reduction Plan," *IEEE Aerospace Conference Paper*, 2018.
- [18] O'Farrell, C., Sonneveldt, B., Karlgaard, C., Tynis, J., and Clark, I., "Overview of the ASPIRE Project's Supersonic Flight Tests of a Strengthened DGB Parachute," *2019 IEEE Aerospace Conference*, 2019.
- [19] O'Farrell, C., Karlgaard, C., Tynis, J., and Clark, I., "Overview and Reconstruction of the ASPIRE Project's SR01 Supersonic Parachute Test," *2018 IEEE Aerospace Conference*, 2018.
- [20] Karlgaard, C., Tartabini, P., Martin, J., Blanchard, R., Kirsch, M., and Thornblom, M., "Statistical Estimation Methods for Trajectory Reconstruction: Application to Hyper-X," Tech. Rep. TM-200-215792, 2009.
- [21] Cruz, J. R., Way, D. W., Shidner, J. D., Davis, J. L., Adams, D. S., and Kipp, D. M., "Reconstruction of the Mars Science Laboratory Parachute Performance," *Journal of Spacecraft and Rockets*, Vol. 51, No. 4, 2014, p. 1185–1196.
- [22] Rabinovitch, J., Griffin, G., Seto, W., O'Farrell, C., Tanner, C., and Clark, I., "ASPIRE Supersonic Parachute Shape Reconstruction: Experimental Results and Comparisons to Simulations," *AIAA Paper*, , No. 2019-1629, 2019.
- [23] Muppidi, S., O'Farrell, C., Van Norman, J. W., and Clark, I. G., "ASPIRE Aerodynamic Models and Flight Performance," *AIAA Paper*, 2019.
- [24] Muppidi, S., O'Farrell, C., Tanner, C. L., and Clark, I. G., "Modeling and Flight Performance of Supersonic Disk-Gap-Band Parachutes in Slender Body Wakes," *AIAA Paper*, 2018.